Propellants, Explosives, Pyrotechnics
SAND2020-0010J

Full Paper

DOI: 10.1002/prep.2019

Modelling the Fluctuations of Reactive Shock Waves in Heterogeneous Solid Explosives as Stochastic Processes

David E. Kittell,*[a] Cole D. Yarrington,[a] Jeremy B. Lechman,[a] David L. Damm,[a] and Melvin R. Baer[a]

Abstract: While current phenomenological burn models are useful for describing the average or bulk reactive flow behaviour of heterogeneous explosives, one fundamental weakness inherent to these models is the loss of detailed microstructural information at the scale of the calculation. In order to include the effects of the microstructure, and in particular the underlying material heterogeneities that influence the build-up to detonation, a new paradigm is put forth for modelling sub-grid, reaction-induced fluctuations (i.e. “hot spots”) at the continuum level. This modelling approach assumes that the reaction rate is stochastic, rather than deterministic, and it uses Langevin-type equations with a mathematical framework built upon Itô calculus and Lambourn’s CIM model for shocked heterogeneous explosives. This approach follows directly from our previous letter, Ref. [1], and is inspired by the probability density function (pdf) methods used in turbulent reactive flows. Here, the stochastic burn model is derived, implemented, and exercised far beyond what has been shown in previous work. New hydrocode simulation results demonstrate the role of stochastic fluctuations during shock initiation; these fluctuations are approximated by collections of discrete particles, that evolve with drift (i.e. deterministic) and diffusion (i.e. stochastic) coefficients. Additionally, the particle values are propagated and averaged to calculate the heat release, yield strength, and material impedance in each computational cell. Hydrocode simulation results further show how the fluctuating hot spot energy may or may not be transmitted to the wave front, and result in a detonation wave-like structure. The fundamental stochastic nature of this model permits simulations to have varying outcomes with the same initial conditions; this allows for go/no-go estimation (e.g., marginal or failed detonations), which might possibly be calibrated using the statistical distributions from real materials. Mesoscale calculations of shocked heterogeneous explosives also show that these fluctuations are physically justified (i.e., Ref. [2]), and it is hypothesized that the pdf functions provide a link between the meso(grain) and continuum scales for practical engineering calculations. Thus, our approach is a paradigm shift for building efficient, reduced order continuum burn models, that represent the sub-grid stochastic behaviour of shocked heterogeneous solid explosives.

Keywords: shock initiation, stochastic process, burn model, mesoscale

1 Introduction

At present, much attention is being focused on the particle/pore scale microstructures of energetic materials (EMs) that appear in a variety of diverse engineering applications (e.g. propulsion, munitions, and device actuation). These applications introduce a broad material variability, where many EMs are heterogeneous mixtures of organic polycrystalline materials, metals and/or polymeric binder with voids and defects [3]. When viewed at the mesoscale (i.e. the scale of the heterogeneities, typically between 0.1 μm and 1 mm), these condensed phase materials exhibit statistically random, i.e. stochastic, microstructures in two- and three-dimensions. One particularly active area of research is in understanding how structural and compositional fluctuations at small length scales modify material properties and behaviour at larger length scales. This, in kind, is related to efforts aimed at novel multiscale modelling frameworks and computational homogenization schemes for stochastic materials, as discussed in recent review papers by Hull *et al*. [4] and Matouš *et al*. [5]. Unfortunately, these approaches are not yet well equipped to handle the strong shock regime, or the ensuing chemical reactions that may occur in EMs. During high explosive (HE) initiation from a mechanical insult, solid mechanics quickly gives way to compressible gas dynamics and nonlinear shock waves at the onset of reaction. Thus, the modelling and simulation of HE initiation brings together several academic disciplines in a unique multiphysics scenario.

A current research effort in EMs is to understand how the observed macroscale responses of detonation and sub-detonative phenomena may or may not be governed by the characteristics of the unreacted microstructures. This objective is motivated by the desire to understand the physical processes occurring at the mesoscale [2], and the promise of leveraging this understanding towards quantifying the safety and performance margins of explosives. For example, it is well known that small defects such as cracks and voids can lead to the formation of reaction sites known as “hot spots” [6,7], which ultimately sensitize these materials. Experimental results also suggest possible links between the stochastic microstructures and shock sensitivity through powder characteristics; some notable trends include the observed changes due to particle size [8], specific surface area (SSA) [9,10], and density [11].

Considering the different numerical modelling and simulation efforts for heterogeneous explosives, many of these can be divided into one of two approaches. One approach is aimed at studying explosives initiation (mesoscale) [12-18], while the other is aimed at studying propagation (continuum) [19-21]. A third approach, atomistic simulations, is acknowledged

[a] *D. E. Kittell, C. D. Yarrington, J. B. Lechman, D. L. Damm, M. R. Baer*
Sandia National Laboratories
P.O. Box 5800, Albuquerque, NM 87185
**e-mail: dekitte@sandia.gov*

here as it pertains to the mesoscale, but it is not discussed in detail. These efforts are summarized in a recent review paper by Handley *et al*. [22], which provides for additional context and identifies some of the knowledge gaps within the field. From this body of literature, it is clear that a large gap exists between the data being generated at the mesoscale and the calibration of continuum burn model parameters; indeed, the current work is focused on finding a link between the meso and continuum scales in some meaningful way. Without a robust scale-bridging link, whatever unique insights that may be gained at the mesoscale will not propagate into the continuum reactive burn models that are currently used in hydrocodes for reactive flow simulations.

Current research [12-22] is progressing to close this knowledge gap from both sides. Finite element analysis (FEA) and Eulerian/Lagrangian hydrocodes, together with modern computing resources allow for an image to computation approach for mesoscale modelling [12]; in this approach, microstructure images are obtained both experimentally and synthetically [13-17]. Pushing mesoscale simulations further, Jackson *et al*. [13] have augmented the energy equation with a power deposition term to include the effects of discrete hot spots. This addition has been shown to increase model fidelity of the shock to detonation transition in a plastic bonded explosive (PBX). On the continuum side, Perry *et al*. [19] show a literal translation of the SURF burn model parameters to more physical quantities. Other recent continuum approaches seek to train an Ignition and Growth-type reactive burn model with surrogate models and/or machine learning techniques [18,20]; however, the training functions are still mostly based on single pore collapse.

While all of these computational techniques have been used in the current efforts, the majority of studies still use the same (i.e. deterministic) hydrocodes with adjusted physics models [22]. It has long been argued by Baer [2,3] that mesoscale simulations should be mined for their rich statistical datasets, and then passed to the continuum level through a probability density function (pdf) of the thermodynamic states. It is anticipated that the pdfs will be measured from mesoscale simulations of a representative volume element (RVE). Unfortunately, this approach requires substantial modifications to the governing continuum-level equations. Baer *et al*. [3] derived the joint pdf transport relationship for randomized deformable media (see Eq. (112) of Ref. [3]), but concede that a direct numerical approach is computationally expensive; also, a set of closure laws are required not unlike the models used in pdf-based turbulence modelling approaches. What is missing from the literature is a mathematically rigorous, yet computationally feasible methodology for homogenizing the meso(grain) scale at the continuum level; specifically, one that addresses the stochastic nature of reactive shock waves and hot spot formation.

Following the pdf methods used in turbulent reactive flows [23,24], a new stochastic burn model will require a particle discretization in order to solve the governing equations. Specifically, the particles are used to represent a pdf distribution that includes extreme states and outliers in the tail, which in turn corresponds to the shocked heterogeneous microstructure through the distribution of the thermodynamic states. However, much work is needed for current particle methods to treat strong pressure gradients with solid, rather than liquid or ideal gas equations of state. Tantalizingly close numerical methods can be found within the granular flow [25] and droplet laden flow [26,27] communities, but it will take time to repurpose these methods for heterogeneous solid explosives. Progress is also being made in stochastic computational modelling that may be relevant to the current work [28]. Finally, dissipative particle dynamics (DPD) and other DPD variants [29,30] have been used to run large three-dimensional particle simulations in order to bridge the gap between fluctuations at the molecular level and the continuum. For example, the stochastic shock to detonation transition (SDT) was recently submitted for publication on a liquid explosive, Nitromethane [31]; however, it is important to note that this is a computationally-intensive framework for homogenizing the atomic and molecular fluctuations. The application of DPD to heterogeneous microstructures is currently an active area of research; see Mattox *et al*. [30].

The objective of this work is to derive a stochastic continuum burn model that is motivated from the top down, i.e. starting from the reactive Euler equations. This model was briefly introduced in a previous letter [1], but it is expanded here to include two additional fluctuating quantities (i.e. yield strength and material impedance) as well as details of its implementation in a one-dimensional hydrocode. Moreover, another objective of this work is to draw possible connections between the meso(grain) and continuum scales through full-field data mining and pdf evolution; however, the execution of such work will be a community endeavour. Overall, the stochastic burn model described herein is exercised to show new model capabilities that are not present in a traditional hydrocode approach. The results of this work demonstrate that a new paradigm is being put forth to capture the effects of reaction-induced fluctuations (i.e. “hot spots”) in shocked heterogeneous solid explosives via stochastic process modelling.

2 Mathematical Model

The approach to stochastic process modelling used here may be summarized as follows: (1) random fluctuations are introduced into a deterministic model via Langevin-type equations with drift and diffusion coefficients, (2) fluctuations are propagated according to the rules of Itô calculus [32], and (3) particle averages are used to solve for the mean flow state. While simple in theory, this approach can introduce significant mathematical complexity; however, such complexity can be managed by choice of a tractable model system. Thus, the application of stochastic process modelling to current burn models (e.g. CREST, SURF, AWSD, SHS, etc. [22]) is beyond the scope of this work. Instead, it is thought that the stochastic nature of the SDT problem will have its greatest influence near the impact surface

and at early times, and a simplified description of the early stages of shock initiation is considered here in a one-dimensional scenario.

James [33] and Lambourn [34,35] performed detailed analyses of the embedded particle-velocity gauge data for sustained shock initiation in a variety of explosives. Following their work, an exact analytic theory was developed that could explain the behaviour of the particle velocity gauge data close to the impact surface. The resulting constant impedance model (CIM) [35] is not only a reasonable mathematical description of the early stages of reaction, but it is also simple enough that stochastic processes may be rigorously applied. The CIM model equations arise from a characteristic analysis, and are generalized in this work to allow for a variable material impedance and a basic strength model. In order to fully encapsulate the approach as outlined in steps (1)-(3) above, this section begins with a derivation of the generalized CIM equations via the method of characteristics, followed by particle averaging, the solution of the Riemann problem, and finally hydrocode implementation.

2.1 Characteristic Analysis

Following the derivation of the CIM model [35], it is assumed that the behaviour of a shocked heterogeneous explosive is governed by the reactive Euler equations; see for example Fickett and Davis, Ch. 4 Eqs. (4.6a) through (4.6d) for a one-dimensional slab geometry and a single reaction rate [36]. Here, pressure is exchanged for the stress tensor, so that the governing equations appear as,

$$\frac{D\rho}{Dt} + \rho \frac{\partial u}{\partial x} = 0, \tag{1}$$

$$\frac{Du}{Dt} - \frac{1}{\rho}\frac{\partial \sigma_{xx}}{\partial x} = 0, \tag{2}$$

$$\frac{DE}{Dt} - \frac{\sigma_{xx}}{\rho}\frac{\partial u}{\partial x} = 0, \tag{3}$$

and

$$\frac{DF}{Dt} = r, \tag{4}$$

where D/Dt is the material derivative, ρ is the density, u is the x-component of the velocity vector, σ_{xx} is the first diagonal element of the stress tensor, E combines the internal energy, e, and heat of reaction, $\tilde{Q}$, into a single expression (i.e. $E = e - \tilde{Q}F$), F is the product mass fraction bound between 0 and 1, and r is the reaction rate. Once the explosive has been shocked, the stress tensor is assumed to lie on the yield surface given by the von Mises yield criteria,

$$\sigma_{xx} = -P - \frac{2}{3}Y, \tag{5}$$

where P is the thermodynamic pressure and Y is the yield strength.

In solving for the characteristic form, the eigenvalues may be greatly simplified by exchanging Eq. (3) for the adiabatic relationship; see for example Ref. [35]. The adiabatic relationship is found in Fickett and Davis, Ch. 4 Eqs. (4.7a) through (4.7c) [36], and it is modified here to include a non-zero yield strength,

$$\frac{DP}{Dt} + \rho c^2 \frac{\partial u}{\partial x} + \frac{1}{\rho\, E_P}\left(\frac{2}{3}Y\right)\frac{\partial u}{\partial x} = \rho c^2 \sigma\, r, \tag{6}$$

where $c^2 = \mathrm{v}^2\,(P + E_\mathrm{v})/E_P$ is the square of the thermodynamic sound speed and $\sigma = (\partial P/\partial F)_{E,\mathrm{v}}/\rho c^2$ is the material thermicity [36]. In order to provide closure to the current model, a Mie-Grüneisen equation of state is assumed to approximate the value of the pressure derivative, E_P. Here, $1/E_P \approx \rho_0\Gamma_0$ where ρ_0 and Γ_0 are the initial density and Grüneisen parameter for the unreacted material, respectively. The term containing the material thermicity is also lumped into an effective heat of reaction, i.e. $Q \triangleq \rho c^2 \sigma$. Finally, the yield strength is assumed to be constant for inert materials; however, it may decrease towards zero as F approaches one to represent the loss of strength due to reaction. Under these assumptions, the reactive Euler equations may be expressed in Lagrangian coordinates as,

$$\frac{D\mathrm{v}}{Dt} - \frac{\partial u}{\partial h} = 0, \tag{7}$$

$$\frac{Du}{Dt} - \frac{\partial \sigma_{xx}}{\partial h} = 0, \tag{8}$$

$$\frac{DP}{Dt} + \left(Z^2 + \frac{2}{3}\rho_0\Gamma_0 Y\right)\frac{\partial u}{\partial h} = Qr, \tag{9}$$

$$\frac{DY}{Dt} = Y_F r, \tag{10}$$

$$\frac{D\sigma_{xx}}{Dt} - \left(Z^2 + \frac{2}{3}\rho_0\Gamma_0 Y\right)\frac{\partial u}{\partial h} = -Qr - \frac{2}{3}Y_F r, \tag{11}$$

and

$$\frac{DF}{Dt} = r, \tag{12}$$

where $\mathrm{v} = 1/\rho$ is the specific volume, $Z = \rho c$ is the material impedance, and h is the aerial mass (i.e. Lagrangian coordinate) defined by $h \triangleq \int_{x_0}^{x} \rho\, d\hat{x}$ [35]. Model characteristics are obtained from the eigenvalues of the corresponding matrix equation [37],

$$\frac{\partial \mathbf{U}}{\partial t} + \mathbf{A}(\mathbf{U})\frac{\partial \mathbf{U}}{\partial h} = \mathbf{S}(\mathbf{U}), \tag{13}$$

where $\mathbf{U}$ is a column vector of the state variables, i.e. $\mathbf{U} = (\mathrm{v}, u, P, Y, \sigma_{xx}, F)^\mathrm{T}$, and boldface notation is used to represent both vectors and matricies. $\mathbf{A}(\mathbf{U})$ is the 6x6 coefficient matrix given by,

$$\mathbf{A} = \begin{pmatrix} 0 & -1 & 0 & 0 & 0 & 0 \\ 0 & 0 & 0 & 0 & -1 & 0 \\ 0 & \Delta^2 & 0 & 0 & 0 & 0 \\ 0 & 0 & 0 & 0 & 0 & 0 \\ 0 & -\Delta^2 & 0 & 0 & 0 & 0 \\ 0 & 0 & 0 & 0 & 0 & 0 \end{pmatrix}, \quad (14)$$

where $\Delta^2 = Z^2 + \frac{2}{3}\rho_0\Gamma_0 Y$ represents the effective material impedance squared, and the source vector, $\mathbf{S}(\mathbf{U})$, is given by,

$$\mathbf{S} = \begin{pmatrix} 0 \\ 0 \\ Qr \\ Y_F r \\ -Qr - \frac{2}{3}Y_F r \\ r \end{pmatrix}. \quad (15)$$

For the characteristic analysis, one works with the homogeneous matrix equation first, i.e. $\mathbf{S} = \mathbf{0}$. The eigenvalues of the coefficient matrix are determined to be $\lambda_i = (0, 0, 0, 0, -\Delta, \Delta)$. The corresponding left and right eigenvector matrices are needed to cast the matrix system into characteristic form. The solution of the right eigenvector matrix, $\mathbf{R}$, and left eigenvector matrix, $\mathbf{L} = \mathbf{R}^{-1}$, have simple analytic closed-form solutions via,

$$\mathbf{R} = \begin{pmatrix} 0 & 0 & 0 & 1 & 1/\Delta^2 & 1/\Delta^2 \\ 0 & 0 & 0 & 0 & 1/\Delta & -1/\Delta \\ 0 & 0 & 1 & 0 & -1 & -1 \\ 0 & 1 & 0 & 0 & 0 & 0 \\ 0 & 0 & 0 & 0 & 1 & 1 \\ 1 & 0 & 0 & 0 & 0 & 0 \end{pmatrix}, \quad (16)$$

and

$$\mathbf{L} = \begin{pmatrix} 0 & 0 & 0 & 0 & 0 & 1 \\ 0 & 0 & 0 & 1 & 0 & 0 \\ 0 & 0 & 1 & 0 & 1 & 0 \\ 1 & 0 & 0 & 0 & -1/\Delta^2 & 0 \\ 0 & \Delta/2 & 0 & 0 & 1/2 & 0 \\ 0 & -\Delta/2 & 0 & 0 & 1/2 & 0 \end{pmatrix}, \quad (17)$$

respectively. Each characteristic equation corresponds to a different eigenvalue, λ_i, and is the result of the following matrix manipulation,

$$\mathbf{L}_i \cdot \left\{ \frac{\partial \mathbf{U}}{\partial t} + \lambda_i \frac{\partial \mathbf{U}}{\partial h} \right\} = \mathbf{L}_i \cdot \mathbf{S}(\mathbf{U}), \quad (18)$$

where $\mathbf{L}_i$ are the row vectors of the left eigenvalue matrix. For the eigenvalues given by $\lambda_{5,6} = \mp\Delta$, the characteristic equations correspond to lines in $t-h$ space having the slope $\mp 1/\Delta$; they are given by,

$$-d\sigma_{xx} \mp \Delta\, du = QdF + \frac{2}{3}Y_F dF. \quad (19)$$

The other four eigenvalues ($\lambda_{1,2,3,4} = 0$) are degenerate, and correspond to lines of $h =$ const. The four additional characteristic equations are given by,

$$-d\sigma_{xx} + \Delta^2\, dv = QdF + \frac{2}{3}Y_F dF, \quad (20)$$

$$-d\sigma_{xx} - dP = \frac{2}{3}Y_F dF, \quad (21)$$

$$dY = Y_F dF, \quad (22)$$

and

$$dF = r\, dt. \quad (23)$$

When yield strength is neglected (i.e. $Y = 0$, $\sigma_{xx} = -P$ and $\Delta = Z$), two of the characteristic equations may be eliminated; the final result is the CIM model, which also serves as the basis for the preliminary stochastic model given by Kittell *et al.* [1].

The primary advantage of expressing the governing equations in characteristic form is that it is both mathematically rigorous yet computationally feasible to take particle averages along the characteristic lines, as will be shown later. By choosing to focus on the fluctuations in heat release (QdF), yield strength (Y), and material impedance (Z) rather than the particle velocity or temperature, the collections of particles follow the material characteristics exactly. Hence, the characteristic equations may be averaged and solved in a straightforward manner.

2.2 Particle Equations

In the Lagrangian coordinate system (i.e., h), individual particle paths are assumed to follow the material characteristic lines of $h =$ const. Along these paths, the particle properties are denoted by an asterisk, e.g. ϕ^*, and may be decomposed as the sum of a mean and fluctuation,

$$\phi^* = \tilde{\phi} + \phi', \quad (24)$$

where $\tilde{\phi}$ is the mean and ϕ' is the fluctuation. For any particle property, the *number-weighted conditional average* is defined by,

$$\tilde{\phi} = \langle\, \phi^* \mid h^* = h \,\rangle, \quad (25)$$

and the mean of the fluctuations is zero, i.e. $\langle \phi' \rangle = 0$. Unlike for turbulence modelling, there are no assumed fluctuations in the particle velocity or in the particle density, such that a number-weighted average is equivalent to one based on mass or volume.

The mechanisms for reaction in heterogeneous solid explosives are thought to be due to local energy concentrations in the microstructure known as hot spots. In light of this view, random fluctuations are introduced into the product mass fraction, F^*, which is bound between 0 and 1, as well as the yield strength, Y^*, and material impedance, Z^*. Following previous work [1], the mass fraction is given by a Langevin equation of the form,

$$dF^* = A_t^*\, dt + B_t^*\, dW_t, \tag{26}$$

where A_t^* and B_t^* are the particle drift and diffusion coefficients, respectively, and dW_t is the Wiener-Lévy process, i.e. a Gaussian random variable with mean zero and variance dt. Here, the Gaussian noise term, dW_t, is used as a preliminary model from the Itô calculus [32], and it assumes that the global reaction rate is an ergodic process. When the diffusion coefficient is set to zero, the drift coefficient takes the role of a traditional burn model such that $dF/dt = A_t$.

For the particle drift coefficient, we appeal to one of the earlier burn models by Lee and Tarver [38] which expresses the concept of hot spot ignition and growth,

$$A_t^* = I\,(1-F^*)^x\,(F^*)^r + G\,(1-F^*)^x\,(F^*)^y\,P^z, \tag{27}$$

where I, x, r, G, y, and z are the model parameters. On the right side of Eq. (27), the drift term is composed of ignition (I) and growth (G) terms, which are applied on a particle basis that is also coupled to the pressure, P. When $F^* = 0$, the drift coefficient is also zero. Physically, a nonzero value is needed for ignition, which may be evolved via the diffusion coefficient having an assumed (i.e. preliminary guess) form of,

$$B_t^* = \begin{cases} 0 & \text{if } \tau \le 0 \\ k_1 \exp(-k_2\,\tau) & \text{if } \tau > 0 \end{cases}, \tag{28}$$

where k_1 and k_2 are model parameters, and the variable $\tau = t - t_{Shk}$ is the time since passage of the first shock. The diffusion coefficient simultaneously eliminates the starting problem, and introduces the stochastic nature of the model; it also expresses hot spot formation as an exponential decay rate. Physically, the distribution of the mass fractions, F^*, is hypothesized to be linked to the statistical distribution of the microstructure, and mesoscale simulations may provide additional insights into modelling the drift coefficient.

Fluctuations are also introduced into the yield strength that depend on F^*. An assumed model form for the yield strength was chosen that approaches zero as the mass fraction approaches one, i.e.

$$Y^* = Y_0\,(1-F^*)^m, \tag{29}$$

where Y_0 and m are model parameters. This strength model represents a constant yield surface for inert materials, that decreases as gaseous products are formed. The Langevin equation to advance Y^* may be obtained from an Itô derivative (see Theorem 4.1.2 in Ref. [32]) as follows,

$$dY^* = \left(A_t^*\,Y_F^* + \frac{1}{2}B_t^{*2}\,Y_{FF}^*\right)dt + B_t^*\,Y_F^*\,dW_t, \tag{30}$$

where Y_F^* and Y_{FF}^* are the first and second derivatives of the yield strength with respect to the particle mass fraction.

Finally, fluctuations are introduced into the material impedance, Z^*. A model description for the impedance requires two equations of state (EOS); one for the unreacted explosive (UR) and one for the reaction products (RP), as well as a mixture rule to combine them. To simplify the current model description, we choose to assume a common density and pressure for both the UR and RP EOS so that the mixture impedance is given by Schmidt's rule [39],

$$\frac{1}{(Z^*)^2} = \frac{1-F^*}{Z_{UR}^2(P,\mathrm{v})} + \frac{F^*}{Z_{RP}^2(P,\mathrm{v})}, \tag{31}$$

where Z_{UR} and Z_{RP} are referred to here as the Z-EOS for the reactants and products, respectively, and $Z^2 = -(\partial P/\partial \mathrm{v})_s$ is equivalent to the square of density times sound speed, i.e. $Z^2 = (\rho c)^2$.

The Z-EOS are calculated following an approach briefly discussed in Ref. [1]. In summary, the specific volume, v, and the specific entropy, s, are taken to be independent thermodynamic state variables. Next, a generalized Mie-Grüneisen form of the EOS is assumed, such that $(\partial P/\partial e)_\mathrm{v}$ is treated as a function of volume alone. Under these conditions, the Z-EOS may be derived from Maxwell's relations, the chain rule, and an arbitrary reference curve in volume as,

$$Z(P,\mathrm{v}) = \sqrt{\left(\frac{\partial P}{\partial e}\right)_\mathrm{v}\left\{P + \left.\frac{de}{d\mathrm{v}}\right|_{ref}\right\} - \left.\frac{dP}{d\mathrm{v}}\right|_{ref}}, \tag{32}$$

where $P_{ref}(\mathrm{v})$ and $e_{ref}(\mathrm{v})$ represent a reference curve in specific volume, such as the Hugoniot or a principal isentrope.

In the current work, Z_{UR} for unreacted solids is given by a Mie-Grüneisen EOS of the form $(\partial P/\partial e)_\mathrm{v} = \rho_0\Gamma_0$ and a reference curve corresponding to a quadratic shock-particle velocity relationship of the form,

$$U_S = C_S + S_1\,u_p + (S_2/C_S)\,u_p^2, \tag{33}$$

where ρ_0, Γ_0, C_S, S_1, and S_2 are the unreacted EOS parameters, U_S is the shock velocity, and u_p is the particle (material) velocity. The reaction products Z_{RP} is calculated from a Jones-Wilkins-Lee (JWL) EOS of the form $(\partial P/\partial e)_\mathrm{v} = \rho\omega$, and the functions $P_{ref}(\mathrm{v})$ and $e_{ref}(\mathrm{v})$ are given by,

$$P_{ref}(\mathrm{v}) = A\exp(-R_1\,\mathbf{V}) + B\exp(-R_2\,\mathbf{V}), \tag{34}$$

and

$$e_{ref}(\mathrm{v}) = \frac{A}{\rho_0 R_1}\exp(-R_1\mathbf{V}) + \frac{B}{\rho_0 R_2}\exp(-R_2\mathbf{V}) - \frac{\varepsilon_0}{\rho_0}, \tag{35}$$

where $\mathbf{V} = \rho_0/\rho$ is the relative volume and ω, A, B, R_1, R_2, and ε_0 are the model parameters. Note that a more recognizable form of the JWL EOS is recovered via the expression $P = P_{ref} + \rho\omega[e - e_{ref}]$, which shows that the JWL model is a subset of the generalized Mie-Grüneisen form, and Eq. (32) may be applied for both the unreacted and reaction products Z-EOS.

Having defined both Z_{UR} and Z_{RP} and by extension Z^* in Eq. (31), the Langevin equation for evolving material impedance may be obtained from an Itô derivative. The result is given by,

$$dZ^* = Z^*_{\mathrm{v}}\, d\mathrm{v} + Z^*_P\, dP + \left(A^*_t\, Z^*_F + \frac{1}{2} B^{*2}_t\, Z^*_{FF}\right) dt + B^*_t\, Z^*_F\, dW_t, \tag{36}$$

where Z^*_{v}, Z^*_P, Z^*_F, and Z^*_{FF} are the partial derivatives of impedance with respect to volume, pressure, and the particle mass fraction, respectively.

The particle values and their governing Langevin Eqs. (26), (30), and (36) may now be substituted into the characteristic Eqs. (19) through (23). Next, a number-weighted particle average is taken along each characteristic, so that the governing equations for the fluctuating reactive flow are given by,

$$-d\sigma_{xx} \mp \langle \Delta^* \rangle\, du = \langle Q dF^* \rangle + \frac{2}{3}\langle Y^*_F dF^* \rangle, \tag{37}$$

$$-d\sigma_{xx} + \langle (\Delta^*)^2 \rangle\, d\mathrm{v} = \langle Q dF^* \rangle + \frac{2}{3}\langle Y^*_F dF^* \rangle, \tag{38}$$

and

$$-d\sigma_{xx} - dP = \frac{2}{3}\langle Y^*_F dF^* \rangle, \tag{39}$$

where two of the particle-averaged characteristics for $\langle dY^* \rangle = \cdots$ and $\langle dF^* \rangle = \cdots$ have been omitted, as the mean values $\langle Y^* \rangle$ and $\langle F^* \rangle$ do not appear in the particle equations; hence, they are decoupled from the solution to the mean flow.

One important result is the self-consistent nature of Eqs. (37)–(39) with previous work, e.g. Refs. [1,35]. When strength is neglected ($Y = 0$, and $\sigma_{xx} = -P$) and the fluctuations are removed from the material impedance ($\Delta^* = Z$), Eqs. (37) and (38) simplify to Eqs. (7) and (8) from Ref. [1]. When it is further assumed that no fluctuations exist in the reaction rate ($F^* = F$) and that the material impedance is constant, then the CIM model is recovered; Eq. (37) simplifies to Eq. (1) from Ref. [35], and Eq. (38) simplifies to the CIM reactive EOS, after performing an integration. Moreover, the "degree of stochasticity" of this current model is controlled by limiting the diffusion of particle values. An exact, deterministic solution is obtained when the diffusion coefficients are set identically to zero. Thus, the analytic constant impedance model (i.e. CIM) solution provides an excellent test for a numerical code. Such CIM-based tests were, in fact, performed during the code development; however, they are not discussed here, as this work is focused on the development of the stochastic model extension.

2.3 Solution of the Riemann Problem

The particle-averaged characteristics in Eqs. (37)–(39) form the governing equations for the stochastic burn model, and may be used to cross any kind of jump discontinuity; e.g. shock wave, fluctuation, or when moving between computational cells. Solving for these discontinuous jumps is the fundamental operation performed in a hydrocode, and it is directly related to the Riemann problem (RP) [37]. Here, a solution to the RP is sought in order to avoid the use of artificial viscosity, which acts to smear all discontinuities over a finite number of cells. Previous attempts to implement a stochastic burn model using artificial viscosity resulted in a small viscous stress throughout the entire shocked material, owing to the particle fluctuations. Alternatively, slope limiters may be explored for hydrocode implementation, but this is beyond the scope of the current work.

In summary of the RP, the state vector, $\mathbf{U}$, is initially discontinuous about an origin, O, as shown in Fig. 1 where it is depicted between two computational cells. This discontinuity leads to left- and right-running waves, as well as to the downstream star region vectors ($\mathbf{U}_{\star L}$ and $\mathbf{U}_{\star R}$), which are unknown. One seeks a solution for the downstream region by matching the velocity and stress states along the $O - t$ axis as discussed in Ref. [37]. This matching condition may be determined by integrating the left- and right-running characteristics in Eq. (37) along the lines $\overline{ac}$ and $\overline{ec}$ in Fig. 1. For hydrocode implementation, an exact solution exists only when the particle-averaged terms (e.g. $\langle \Delta^* \rangle$) are constant. This may be assumed across small time steps, i.e., δt. Thus, the integrals of the characteristic equations are solved with constant particle-averaged values initialized at the beginning of each time step; these values are marked with a subscript to indicate the left and right initial conditions, i.e. $\langle \phi^* \rangle_L$ and $\langle \phi^* \rangle_R$, respectively.

Taking the integral of Eq. (37) over lines $\overline{ac}$ and $\overline{ec}$ yields two equations in two unknowns; the solution for velocity and stress is given by,

$$u_\star = \frac{\Phi_1 - \Phi_2}{\langle \Delta^* \rangle_L + \langle \Delta^* \rangle_R}, \tag{40}$$

and

$$-\sigma_{xx,\star} = \frac{\langle \Delta^* \rangle_R\, \Phi_1 + \langle \Delta^* \rangle_L\, \Phi_2}{\langle \Delta^* \rangle_L + \langle \Delta^* \rangle_R}, \tag{41}$$

where $\langle \Delta^* \rangle_L$ and $\langle \Delta^* \rangle_R$ are the initial left and right particle-averaged effective material impedances, and the functions Φ_1 and Φ_2 are used to simplify the expressions; they are given by,

$$\Phi_1 = \left(-\sigma_{xx} + \langle \Delta^* \rangle u + \langle Q dF^* \rangle + \tfrac{2}{3}\langle Y^*_F dF^* \rangle\right)_L, \tag{42}$$

and

$$\Phi_1 = \left(-\sigma_{xx} - \langle \Delta^* \rangle u + \langle Q dF^* \rangle + \tfrac{2}{3}\langle Y^*_F dF^* \rangle\right)_R, \tag{43}$$

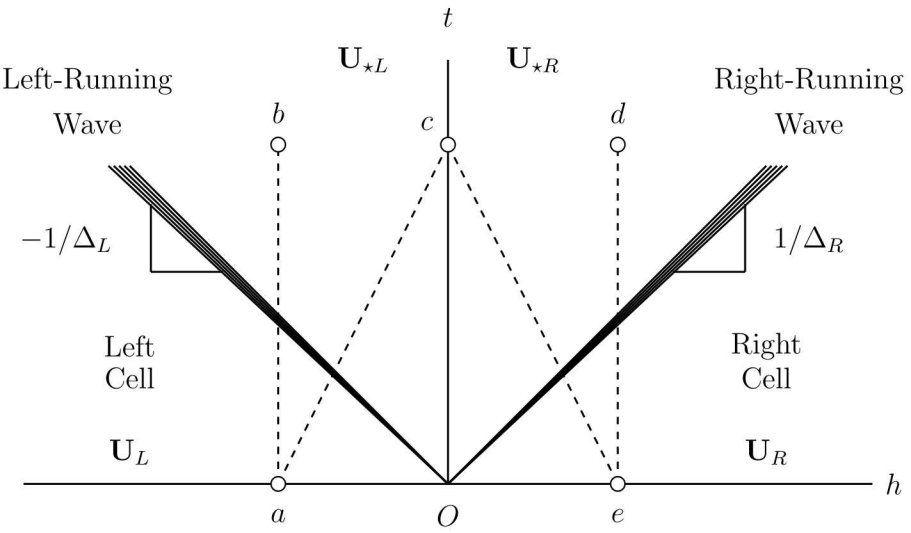

Figure 1. Diagram for the Riemann problem. Characteristic equations are integrated along lines $\overline{ac}$ and $\overline{ec}$ to solve for a common velocity and stress state at point c. All other values may be solved by integrating the characteristic equations along lines $\overline{ab}$ and $\overline{ed}$.

for the left and right sides, respectively. Note that Eqs. (40)–(43) simplify to Eqs. (9)–(12) in Ref. [1] when strength is neglected and the fluctuations are removed from the material impedance.

To determine all other values inside of the star region, the remaining characteristic equations are integrated over lines $\overline{ab}$ and $\overline{ed}$ in Fig. 1. The resulting downstream pressures and volumes are found to be,

$$P_{\star L} = P_L - \left(\sigma_{xx,\star} - \sigma_{xx,L}\right) - \tfrac{2}{3}\langle Y_F^* dF^* \rangle_L, \qquad (44)$$

$$P_{\star R} = P_R - \left(\sigma_{xx,\star} - \sigma_{xx,R}\right) - \tfrac{2}{3}\langle Y_F^* dF^* \rangle_R, \qquad (45)$$

$$\mathrm{v}_{\star L} = \mathrm{v}_L + \frac{\sigma_{xx,\star} - \sigma_{xx,L} + \langle Q dF^* \rangle_L + \frac{2}{3}\langle Y_F^* dF^* \rangle_L}{\langle (\Delta^*)^2 \rangle_L}, \qquad (46)$$

and

$$\mathrm{v}_{\star R} = \mathrm{v}_R + \frac{\sigma_{xx,\star} - \sigma_{xx,R} + \langle Q dF^* \rangle_R + \frac{2}{3}\langle Y_F^* dF^* \rangle_R}{\langle (\Delta^*)^2 \rangle_R}. \qquad (47)$$

Thus, the values obtained inside the star region are determined by simple algebraic relationships. In this work, Eqs. (40)–(47) were programmed into an exact Riemann solver and they are applied at the mesh faces using a research hydrocode. The numerical method is referred to here as the "method of particle-averaged characteristics" or MOPAC for the remainder of the work. Further details of the hydrocode implementation are discussed next in Sec. 2.4.

2.4 Hydrocode Implementation

The stochastic SDT problem was simulated in a one-dimensional research hydrocode, tailored for a flyer plate impact scenario into an explosive target. This setup requires a finite mesh discretization in aerial mass coordinates, i.e., δh, and three fundamental code operations, described as follows. The first operation is a time integration to advance the Langevin equations via forward Euler discretization. For ODEs, this is trivial; however, for stochastic differential equations (SDEs) the drift coefficients must be included. For example, Eq. (26) may be integrated as,

$$F_{i+1}^* = F_i^* + A_{t,i}^* \, \delta t + B_{t,i}^* \, \delta t^{1/2} \, \xi, \qquad (48)$$

where the subscript i is the cycle number, δt is the time step, and ξ is a random number with mean zero and a standard deviation of one; see Ref. [32] for additional details. A pseudo random number generator (PRNG) was obtained under the GNU LGPL license based on a numerical method from Ref. [40]. The PRNG seed value is specified by the user in an input deck; each seed determines a unique sequence of pseudo-random numbers, which enables code repeatability.

After the particle update and subsequent particle averaging in each computational cell, in step two Eqs. (40)–(47) are used to solve for the downstream star region values, which are stored as face-centred values. Finally, in step three, the cell-centred values are updated using the two adjacent faces. While a variety of different numerical methods are available (notably Godunov and HLLC), a global scheme based on the random choice method (RCM) [37] was found to allow the shock front to remain steep, while also mitigating the smearing of particle fluctuations. In summary of this technique, a weighted Monte Carlo method determines whether to update the cells based on the left face, right face, or current value (i.e. no change). For a sufficiently small cell size, δh, the trajectory of an inert shock wave converges to the analytical solution.

Model parameters for an inert flyer and explosive target are listed in Table 1 and are used throughout this

work. Additionally, the coordinate system is chosen so that the material interface is located at $h = 0$ g/cm^2 (note that the materials do not move in h-coordinates). Geometry and model choices are summarized as follows: the flyer is 10 mm thick with an initial velocity of 1.0 km/s; it resembles the EOS of a low impedance cast acrylic sheet, Perspex©. The target is 7 mm thick with zero initial velocity; it resembles the EOS parameters of an HMX-based polymer bonded explosive, PBX9501. The drift and diffusion model parameters were chosen in order to highlight some of the novel stochastic material behaviours, although they have yet to be refined and calibrated to the physical hot spot processes. These dimensions and initial conditions are used for all baseline simulations; however, some variations in the flyer velocity, flyer thickness, and numerical settings are explored in the results section.

3 Simulation Results

Simulation results for a representative flyer plate impact scenario are shown in Fig. 2 using the model parameters from Table 1. The flyer and target are separated by a vertical dashed line, and the flyer velocity of 1.0 km/s yields an initial stress state and particle velocity of 1.93 GPa and 0.37 km/s, respectively. The shock wave originates at the material interface without any signs of reaction; at time zero, it is a square wave with a constant value. However, some curvature is observed ~1.0 μs after impact as shown in Fig. 2(a). Reaction then develops into a "hump" or "spike" behind the leading wave, similar to what is observed in the embedded velocity gauge data [34]. We note that while experimental data more closely resembles that of a rounded "hump," the "spike" is a characteristic of the Lee-Tarver reaction rate [38], and this particular feature could be improved via adaptation of a current burn model [22]. Regardless, the effective heat release allows the material impedance to grow, so that energy is propagated forward along the right-running characteristics; this increases the strength of the leading wave. The end result is a detonation wave-like structure appearing ~1.8 μs after impact, as observed in Fig. 2(d).

While the pressure and velocity results might appear to have been produced from a traditional hydrocode, some unique stochastic behaviours are observed. At early times, e.g. Fig. 2(a,b), the velocity and pressure curves are very smooth, yet at later times, e.g. in Fig. 2(c,d), there are sharp fluctuations behind the leading wave. These reaction-induced fluctuations are stochastic, and they are never the same twice (provided a different seed value is input to the PRNG). In Fig. 2, the mesh resolution and number of particles per cell were set at 5e-4 g/cm^2 and 200, respectively. This baseline impact simulation was rerun 50 times using different seed values chosen from a list of prime numbers, in order to estimate the model-based variability between runs.

For 50 repeated simulations with the same initial conditions, the mean flow and variance were calculated in each cell. Fig. 3 shows the mean flow and 2σ variance

Table 1. Model parameters used to represent the inert flyer and explosive target materials.

Model	*Parameter*	*Flyer*	*Target*
MG	ρ_0, g/cm^3	1.186	1.86
EOS	Γ_0	0.97	1.1
	C_S, km/s	2.598	2.686
	S_1	1.516	2.256
	S_2	0	-0.483
Strength	Y_0, GPa	0	0.1
	m	0	3
JWL	ω	0	0.38
EOS	A, GPa	0	852.4
	B, GPa	0	18.02
	R_1	0	4.6
	R_2	0	1.3
	ε_0, GPa	0	10.2
Eff. Ht.	Q, GPa	0	8
Drift	I, μs^{-1}	0	0.01
(i.e. A_t^*)	x	0	2/9
	r	0	2/3
	G, (GPa)$^{-z}$ μs^{-1}	0	0.5
	y	0	2/3
	z	0	2
Diffusion	k_1, μs$^{-1/2}$	0	0.01
(i.e. B_t^*)	k_2, μs^{-1}	0	0.1

(i.e. 95% prediction interval or PI) in velocity and pressure at 1.66 μs after impact; this time corresponds to the same output as Fig. 2(c). Variations in pressure and velocity are the largest at the reaction "spike" located near $h \approx 0.6$ g/cm^2, and approximately zero around the material interface. For a reaction-induced fluctuation model, inert shock waves will have zero variability in the mean; however, a small uncertainty always exists at the wave front due to the RCM global scheme used. Much of the 95% PI shown in Fig. 3 is close to zero, hence these regions of the calculation are relatively unaffected by the particle fluctuations.

Compared to Fig. 2(c), the mean particle velocity and pressure in Fig. 3 are smooth functions, as the results are averaged over 50 different runs. These smoothed distributions are analogous to the pdfs obtained when modelling turbulent reactive flows. Moreover, the mean flow and variance shown in Fig. 3 are well-behaved functions, and will converge to a theoretical solution as the number of simulations approaches infinity. One could solve for the governing pdf equations directly; this is done by transforming the Langevin description from Itô calculus (differential form) into an equivalent set of Fokker-Planck equations (integral form). However, that derivation has yet to be attempted for the current model. Note that the MOPAC numerical scheme would also change in order to solve the set of governing Fokker-Planck equations.

Another observation from Fig. 3 is that the mean and variance come from a single set of stochastic model parameters. This type of reaction-induced variability

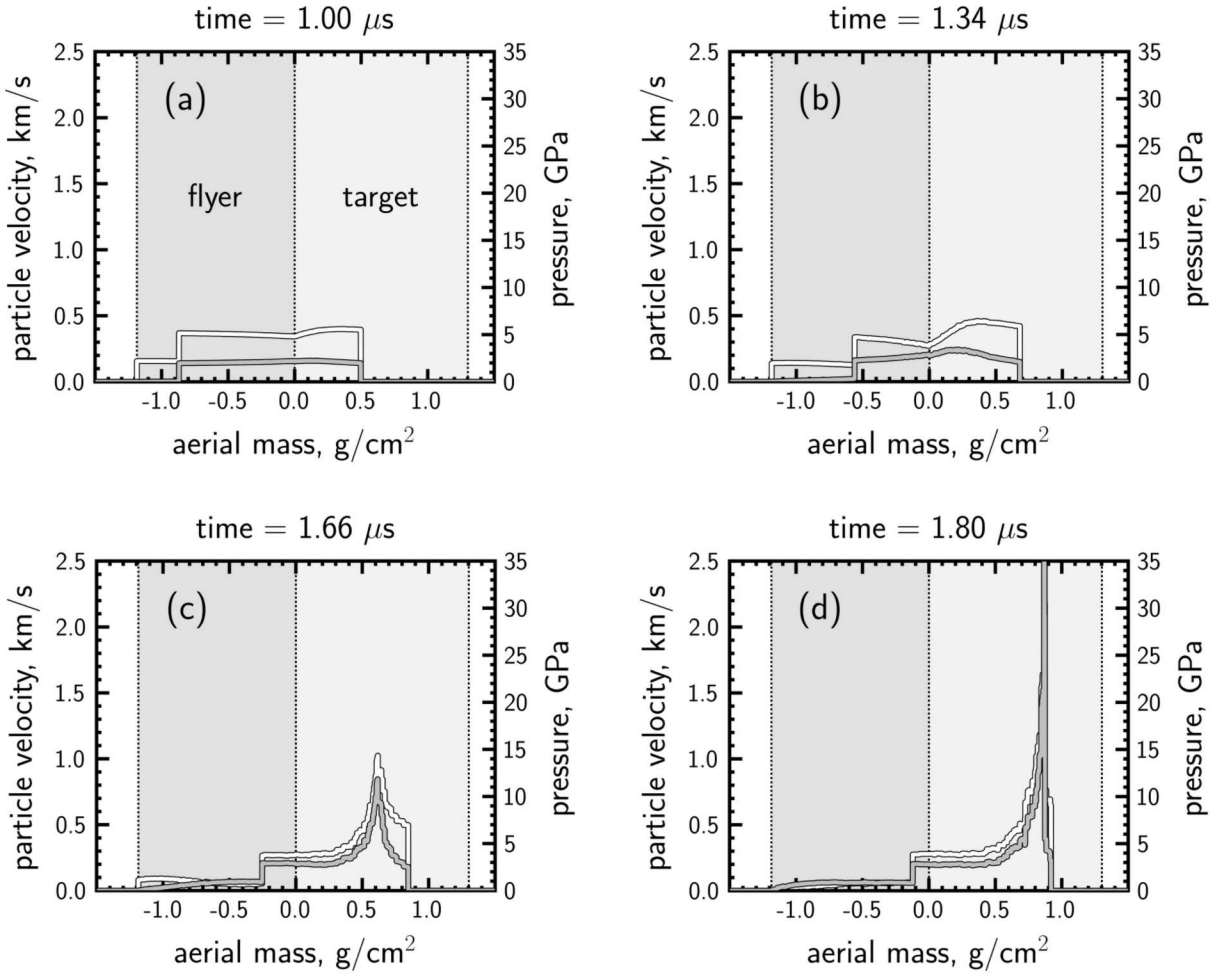

Figure 2. Simulation output for a one-dimensional flyer impact in aerial mass coordinates. The results show the mean particle velocity (light curve) and pressure (dark curve) at four different times, labelled (a) through (d); flyer and target model parameters may be found in Table 1.

cannot be obtained from a traditional hydrocode with a deterministic burn model. That is, variation of the burn model parameters provides a measure of the epistemic uncertainty; i.e., error due to the unknown parameter values. Here, the stochastic Itô calculus is used to inform the *process-based variability*, i.e. aleatoric error that is thought to result from the dynamic formation of interacting hot spots. For uncertainty quantification, these two sources of error (epistemic vs. aleatoric) are fundamentally different. Moreover, there may be a direct connection between the process-based variability and current high-fidelity mesoscale simulations; such simulations are thought to be able to provide data that can be used to quantify the aleatoric error, and they are envisioned to fit the drift coefficient model parameters.

Evidence for a randomized, aleatoric error is often visible in the fluctuations of particle velocity data, e.g., [2,41]; however, this observation is usually dismissed as the SDT experiments are highly repeatable and the fluctuations are relatively small. Mathematically, the variance may be adjusted to any size by controlling the relative weights of the drift versus diffusion coefficients in Eq. (26). For example, a reduction in the parameter k_1 will decrease the size of

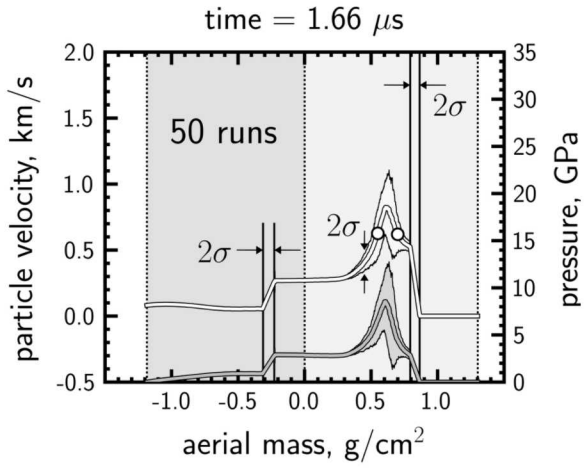

Figure 3. Mean particle velocity and pressure (light and dark curves, respectively) from 50 different simulations with the same initial conditions. The shaded envelopes show two standard deviations about the mean. The QOI is indicated as the region between the two white dots.

the envelope near the reaction "spike" in Fig. 3. Thus, a stochastic model need not lead to highly unpredictable results. Similarly, the randomized stochastic nature of shock initiation may be obscured by the available continuum-level gauge measurements, or possibly it is cancelled out by the strong deterministic growth of reaction after hot spot coalescence.

3.1 Numerical Convergence Studies

Numerical solutions of stochastic differential equations have both weak and strong convergence [42]. Weak convergence relates to the mean values obtained from the numerical method, whereas strong convergence relates to the particle values and their distributions. It is difficult to bound the different numerical errors in a mathematically rigorous way; however, some empirical results may be given to show that the simulations in Figs. 2 and 3 are converging with respect to their mean and fluctuations.

Numerical parameters consist of the mesh resolution (δh), number of particles per cell (nppc), and the number of repeated simulations (nsim). Note, the time step is not considered as it is calculated from the Courant limit and a 60% safety factor [37]. To explore the effects of these numerical settings on convergence, a quantity of interest (QOI) must be defined. Here, the QOI is the mean velocity between $h = 0.55$ g/cm^2 and $h = 0.7$ g/cm^2 at 1.66 μs after impact; this spatial-temporal domain is indicated in Fig. 3 between the two dots, and corresponds to the mean velocity across the reaction "spike." At 1.66 μs, the reaction is accelerating towards the detonation wave-like structure in Fig. 2(d), with an average velocity in the spike around 700 m/s.

Results for three convergence studies are shown in Figs. 4 through 6, corresponding to the range of parameter values listed in Table 2. Case (i) varies the mesh resolution while using 100 particles per cell and 25 repeated simulations. The mean QOI and its variation are shown in Fig. 4, as the solid line and shaded region, respectively. From Fig. 4, the mean and variance are observed to converge around $\delta h =$ 1e-3 g/cm^2, and this mesh resolution is often used for a wide range of different impact simulations. A finer mesh resolution of 5e-4 g/cm^2 may be used to ensure the convergence of simulation results, e.g. in Figs. 2 and 3. It is also possible to convert $\delta h =$ 1e-3 and 5e-4 g/cm^2 into Eulerian mesh coordinates at time zero; there, the corresponding mesh resolutions are 186 and 372 zones per mm, respectively, using ρ_0 from the explosive EOS.

Experience has shown that mesh resolution is the primary driver for weak convergence. Likewise, the number of particles per cell is a significant factor for strong convergence [23]. As the particle count increases, the accuracy of the particle-averaged quantities, e.g. $\langle \phi^* \rangle$, improves. In Case (ii), the QOI was computed using 5 to 200 particles per cell at a fixed mesh resolution, as shown in Fig. 5. However, the mean QOI and variance are approximately constant for this study. Even with a lower particle count, e.g. 5 per cell, there are a sufficient number of particles between $h =$ 0.55 and 0.7 g/cm^2 to be statistically significant. Using a nppc of 5 yields 750 particles contained inside this spatial domain; hence, this QOI is not as informative for strong convergence. Preliminary work on stochastic burn models [1] assumed 64 particles per cell as a rule of thumb, based loosely on the results from Ref. [42]. Future particle studies should examine a cell-based convergence metric, rather than one based on the mean flow.

Table 2. Summary of three convergence studies for the quantity of interest (QOI) as indicated in Fig. 3.

Case	δh, g/cm^2	nppc	nsim[a]	Total Runs[b]
(i)	vary	100	25	1250
(ii)	1e-3	vary	25	1000
(iii)	5e-4	200	Vary	50

[a]Number of simulations averaged to calculate the QOI.
[b]Total number of simulations used in the study.

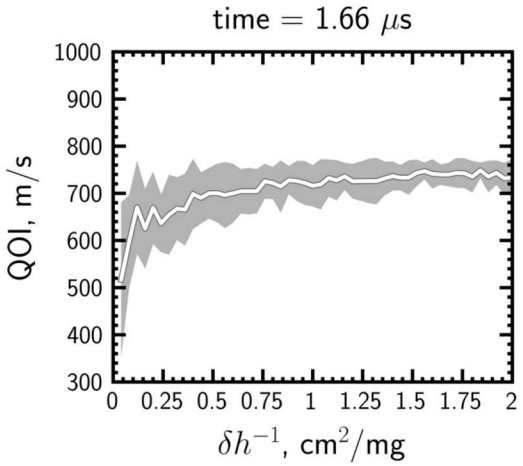

Figure 4. Convergence study while varying the mesh resolution; see Table 2 Case (i). The mean value is a solid white line and the variance is shaded.

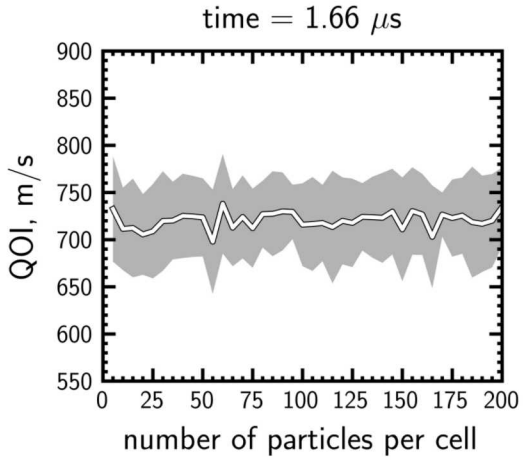

Figure 5. Convergence study varying the number of particles per cell; see Table 2 Case (ii). The mean value is a solid white line and the variance is shaded.

Finally, stochastic simulations at fixed initial conditions may be repeated to estimate variations in the predicted outcome. Case (iii) computes the QOI as the number of simulations is increased from 5 to 50; refer to Fig. 6. This study was performed at the highest mesh resolution of 5e-4 g/cm^2 and 200 particles per cell. Here, the QOI mean and variance are relatively constant, yet there is some evidence of convergence around 25 simulations. Moving from 5-25 to 25-50 simulations, there is less variability observed in the mean QOI and its variance. This result hints at strong convergence, as will be discussed next.

In order to visualize the difference between 10 and 50 simulations, the mean and its variance from Fig. 3 were recalculated using only 10 runs in Fig. 7. A direct comparison between Figs. 3 and 7 reveals that while the mean flow may be smooth in both cases, the variance and 95% PI are not. This result confronts the analyst with a new decision to make; to what level of accuracy or statistical significance should the simulations be performed at? If the mean flow is most important, weak convergence is sufficient. However, if the analyst requires an accurate statistical representation of the thermodynamic states, then strong convergence is required. These issues must be balanced, especially as the dimensionality of the stochastic burn model is increased from one to two, and ultimately three dimensions. These empirical results also suggest that the one-dimensional impact simulations are adequately converged with a mesh resolution of 1e-3 g/cm^2, 100 particles per cell, and 25 repeated runs. Such conclusions are influenced by the need to minimize the CPU cost for processing thousands of runs. Note that when compared to the computationally-intensive framework of dissipative particle dynamics, the potential cost savings is enormous.

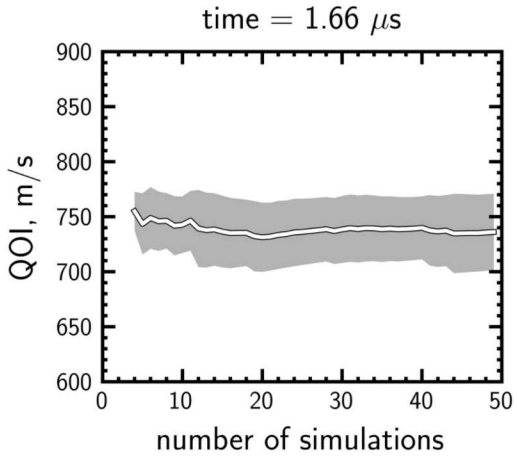

Figure 6. Convergence study varying the number of repeated simulations; see Table 2 Case (iii). Mean QOI is a solid white line and the variance is shaded.

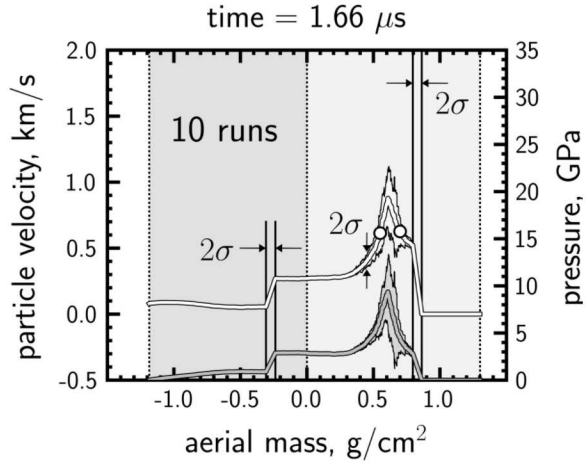

Figure 7. Particle velocity and pressure from 10 different simulations at the same initial conditions; compare to Fig. 3, showing an average over 50 runs.

3.2 Particle Distributions

Results from a stochastic burn model also include the distributions of particle values and their pdfs. Each cell holds a pdf distribution, and an overall pdf distribution exists for the shocked material as well. Collections of the mass fractions, F^*, are shown in Fig. 8 as dots, and the mean value as a solid line. This sequence corresponds to the same simulation and time output from Fig. 2. In summary, these particle results help to visualize how Eq. (28) introduces the stochastic fluctuations right behind the leading shock (representing hot spot initiation), and how at later times the mean pressure in Eq. (27) dominates to drive the mass fraction values to one.

Here, the drift and diffusion coefficients in the Langevin Eq. (26) naturally bridge the gap between HE initiation (stochastic) and propagation (deterministic). Moreover, the particle fluctuations, which have their greatest variability in Fig. 8(a,b), do not appear as fluctuations in the mean flow velocity and stress states until later times. This is because the effective heat release is tied to the change in the particle values, i.e. $\langle QdF^* \rangle$, rather than the values themselves. Thus, the heat release is greatest when the reaction gradient is most steep, e.g. Fig. 8(c,d). One consequence is that the experimental measurements might not be able to capture these complex particle fluctuations at early times. Since instrumented HE experiments usually measure the bulk velocity or stress state, our model results indicate that the largest particle variations will not be observed until much later, as the growth of reaction takes over. While experiments are not yet able to sample these early time mass fraction distributions, it is possible to extract them from high-fidelity mesoscale simulations. Such an approach requires full-field data mining and pdf evolution, as will be discussed later.

Another particle-based result is the distribution of the yield strength, Y^*, as shown in Fig. 9. In the current model, there is a tight coupling between F^* and Y^* through Eq. (29), but this is not a one-to-one mapping. The Itô derivative propagates noise from the drift term, B_t^*, such that Y^* is also a stochastic random variable with its own drift and diffusion coefficients. In summary of the yield strength results, pristine HE has a maximum value of 100 MPa that “degrades” to zero following a

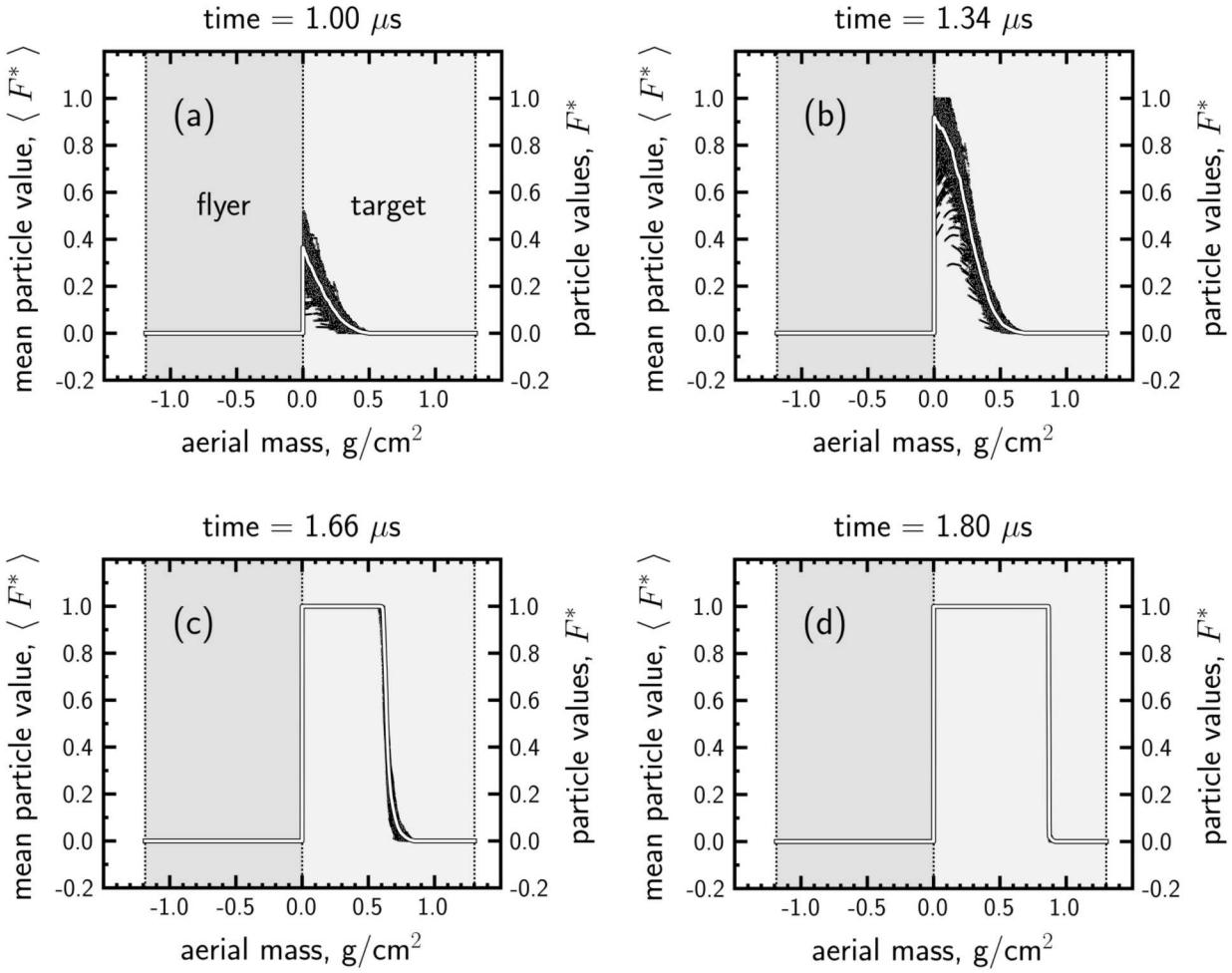

Figure 8. Particle values (dots) showing the distribution of the mass fractions, F^*, at four different times, labelled (a) through (d); results correspond to the same simulation output and time sequence from Fig. 2. The mean value is given as a solid white line.

shock. Loss of strength is caused by reaction, i.e. when gas phase products are formed. Since the governing model for yield strength contains a depletion term with $1 - F^*$, Figs. 8 and 9 bear a strong resemblance to each other.

In the current model, all of the Langevin Eqs. (26), (30), and (36) are placeholders for a more generalized stochastic burn model. Some of the current expressions are phenomenological, and should be informed by the actual statistical distributions. This is especially true for Eqs. (29) and (30); these fluctuations were originally introduced into the yield strength in anticipation of using the stochastic model for low-pressure, accident-type impact scenarios. Although such yield strength fluctuations are less important for SDT, they do allow for comparisons between the continuum and the mesoscale via joint pdfs (or jpdfs).

The distributions shown in Figs. 8 and 9 are marginal pdfs. Since the marginal pdfs may be correlated to each other in some significant way, only jpdfs provide a complete picture of the shock initiation process; examples of jpdfs may be found in Ref. [3]. Results for the particle impedance values were also calculated, and the magnitude of the fluctuations was found to be small in comparison to the magnitude of the mean. Thus, the particle impedance results are not shown.

3.3 Stochastic Initiation

Following the model derivation, implementation, and numerical convergence studies, perhaps the most interesting application of a stochastic reactive burn model is simulating threshold conditions, marginal detonation waves and detonation failure. Note: the term “threshold conditions” is used here, broadly speaking, to cover both thin pulse flyers (geometry-dependent) and supported (geometry-independent) shock initiation. Unlike continuum reactive burn models that are tuned to sustained growth, the fluctuating particle values allow for go/no-go outcomes at the same impact pressures, and model parameters. From a mathematical point of view, there is a competition between wave steepening and release; unfavourable characteristic gradients contribute to failed detonation waves for a marginal shock input.

Such novel initiation behaviour has been previously shown by constructing a Pop plot for the successful SDT cases, and tallying the no-go’s on the right side of the plot for detonation failure (i.e. Fig. 3 of Ref. [1]). Note: a description of the Pop plot may be

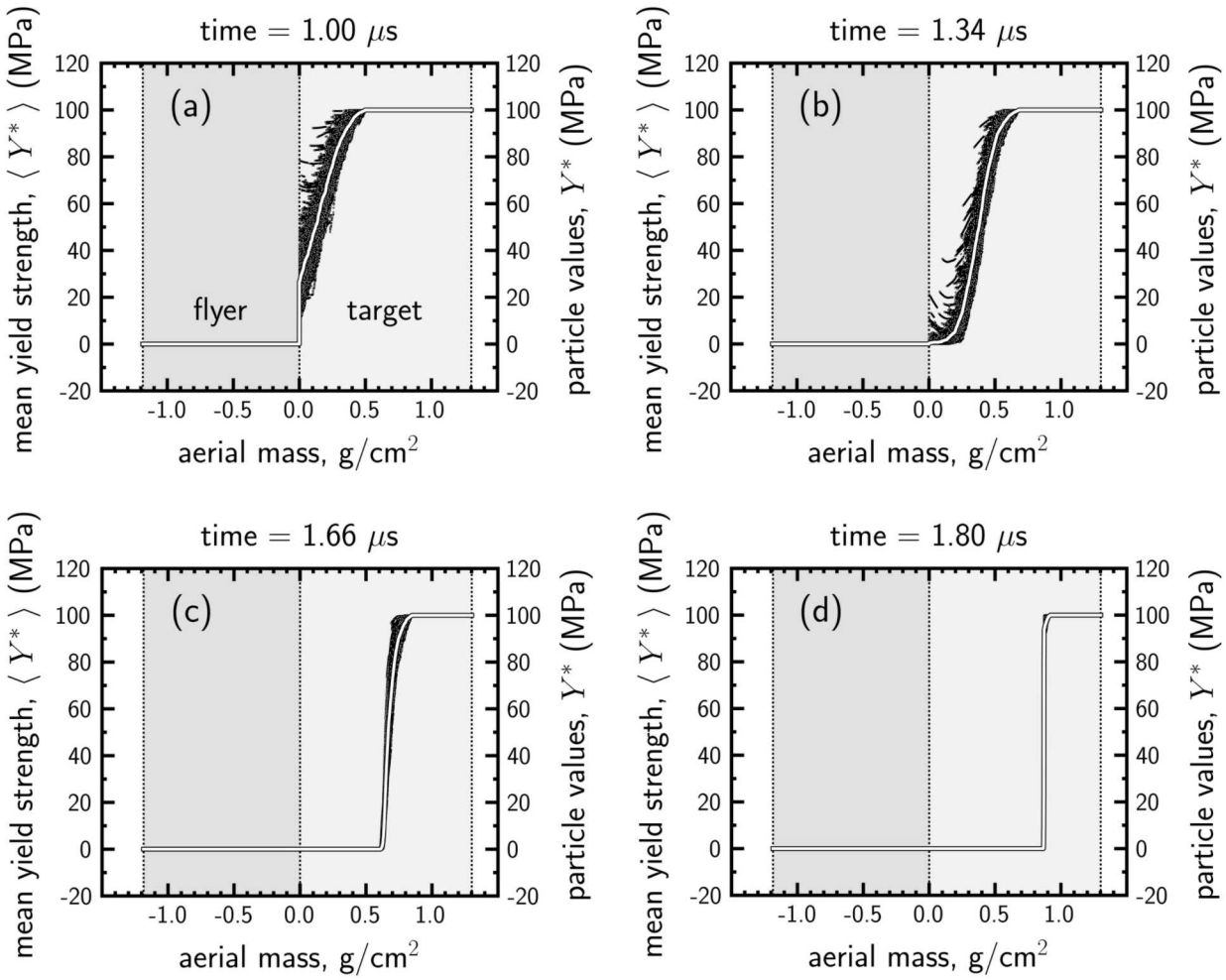

Figure 9. Particle values (dots) showing the distribution of the yield strength, Y^*, at four different times, labelled (a) through (d); results correspond to the same simulation output and time sequence from Fig. 2. The mean value is given as a solid white line.

found in Ref. [43]. Here, the improved stochastic burn model is exercised by mapping the distribution of outcomes from a 10 mm thick flyer impacting a 60 mm thick target at nine different flyer velocities: 1000, 900, 800, 700, 600, 500, 400, 350, and 300 m/s. Each flyer velocity was simulated 50 times using a different seed value for the PRNG, and the simulation results are reported in Fig. 10. The left and right sides of Fig. 10 share the same y-axis in pressure, while the no go cases are reported both as a frequency distribution (solid line) and a black and white colour map to highlight the estimated initiation pressure threshold.

In summary of the Pop plot, it is similar to the one found in Ref. [1] in many ways. For example, the variation in run distance (Fig. 10, left) increases as the shock pressure decreases. This result reinforces the idea that prompt initiation (i.e. higher shock strength) is more deterministic, whereas the low-pressure regime is more stochastic due to the greater influence of discrete hot spot formation and interactions with material microstructural heterogeneities. Qualitatively, the linear trend between shock pressure and run distance in log-log space is also recovered, which is the actual behaviour found in real materials. As a comparison to previous work, the current Pop plot and the one in Ref.

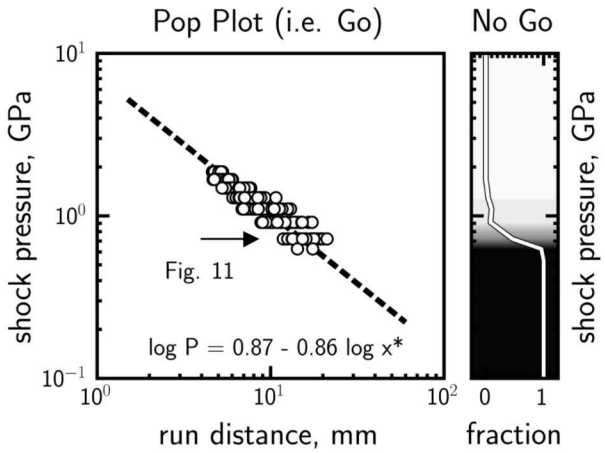

Figure 10. Pop plot and no go fraction for nine different flyer velocities; distributions are based on 50 simulations at each impact condition. An arrow indicates the location of a comparison study shown Fig. 11, and a black and white colour map is used to highlight the estimated initiation threshold.

[1] differ in the sharpness of transition from go to no-go, the linear fit, and also in the behaviour of high-pressure simulation results. Moving from the original to the current model, the intercept has changed from 0.98 to 0.87 and the slope has changed from -0.83 to -0.86. Much of the vertical shift in pressure is attributed to the inclusion of yield strength.

The range of shock pressures in Fig. 10 lie between 1.87 and 0.53 GPa; shock initiation was never observed below 300 m/s for a 10 mm thick flyer, so the no-go fraction of 1.0 was extended to zero pressure for illustration. The Pop plot pressure range is lower than what is observed for a typical PBX, but the stochastic burn model has yet to be refined and calibrated. The EOS parameters are similar to real materials, whereas the drift coefficients (i.e. I and G), diffusion parameters (i.e. k_1 and k_2), and effective heat of reaction (i.e. Q) were adjusted to observe a prompt detonation at a flyer velocity of 1.0 km/s. Consequently, the shock pressure had to be reduced below 1 GPa in order to observe the marginal detonation waves shown in the results. Here, the run distance to detonation is calculated from the peak density in the reactive shock wave – peak density does not appear until after the formation of the detonation wave-like structure. When density exceeds 4.0 g/cm^3 (a user defined value), the location is recorded for the Pop plot; if the density stays below 4.0 g/cm^3, then it is determined to be a sub-detonative response.

Throughout testing, it was found that the Courant-limiting time step drops significantly at higher pressures; hence, flyer velocities above ~1 km/s cannot be fully explored without a stiff solver, and this has yet to be implemented in the hydrocode. Furthermore, the solution algorithm relies on a forward scheme rather than a predictor-corrector. The shock pressures shown in Fig. 10 are determined by the effective impedances at the beginning of each time step; a corrector step is needed to achieve the same shock pressures that lie on the Hugoniot curve. Specifically, the hydrocode pressures are lower than the Hugoniot curve by 1.03 and 0.13 GPa at 1000 and 300 m/s, respectively. These limitations are tied to the underlying CIM model assumptions [35], yet this simplified model description allows for a practical model implementation in a research hydrocode.

In light of the preliminary nature of Fig. 10, two of the threshold (i.e. marginal ignition) cases are shown in greater detail to explore how particle distributions may or may not lead to a successful shock initiation. Specifically, two runs at 400 m/s are shown in Fig. 11; the results consist of the simulated particle velocity gauge data (i.e. Fig. 11(a,b)), the particle distributions for an interior point in the explosive (i.e. Fig. 11(c,d)), and higher order moments of the particle distributions (i.e. Fig. 11(e,f)). Each successive plot reveals greater insight into why the detonation failed.

Concerning the gauge data, 12 cell locations at 1.61 mm increments into the explosive show the build-up to detonation; Fig. 11(a,b) is similar to the type of data that is measured experimentally [33]. For this particular case, the maximum particle velocity or reaction "spike" does not appear until much later in time than it does for the prompt initiation cases. The reaction begins to accelerate around 5 μs, but it is arrested in one case and not the other. Note that while the target is 60 mm thick, these simulations end when the detonation front achieves a maximum density of 4.0 g/cm^3. Also, the last 2 gauges in Fig. 11(b) show evidence of the release wave from a 10 mm thick flyer rear surface.

To investigate the role of pdf evolution, Fig. 11(c,d) shows the individual values and mean of F^* located in the fourth velocity gauge of Fig. 11(a,b); this cell stays in the shock compressed state for ~3 μs before the release wave arrives from the back of the flyer. Release waves are unavoidable in the current hydrocode; a finite flyer thickness was chosen to be 10 mm, which results in a similar calculation as a sustained shock initiation experiment, while balancing the CPU cost based on the number of cells. We note here that the original Pop plot from Ref. [1] was greatly affected by these release waves, much more than in the current results shown in Fig. 10. Regardless, before the release wave arrives, Fig. 11(c,d) shows that different amounts of stored chemical energy were passed forward to the shock front along the right-running material characteristics. The mean value, $\langle F^* \rangle$, is higher in Fig. 11(c) than it is in Fig. 11(d); a dashed line is drawn at $\langle F^* \rangle = 0.7$ as a guide to the eye to observe the different values.

Not only are the mean values higher in the 'go' outcome, the particle values evolve into two different, non-uniform pdf distributions. Two of the higher-order moments (variance and skewness) complete the full picture of detonation failure. When the shock wave first passes over the cell located at 4.81 mm, there is a low variance but positive skewness. Positive skewness indicates that the tail of the pdf distribution is weighted on the right; i.e., a higher value for the skewness indicates more F^* outliers above the mean (i.e. more "hot" outliers), which can begin to grow the pressure faster. The no go case has lower skewness and thus fewer "hot" outliers. However, the skewness always trends downward in time as the particles react. Thus, at later times, the skewness drops and the tail of the pdf distribution shifts to the lower end where reaction has stalled. When the release wave arrives at the No. 4 gauge location around 5 μs, the distribution is effectively frozen in time. Note, when the skewness passes through zero, the distributions momentarily appear to be Gaussian; the time of zero skewness occurs in the 'go' case around 5 μs, but it is about 1 μs earlier for the 'no-go' case. Thus, pdf evolution is greatly influenced by the tails, and in fact the tails of the pdf distribution may hold the key to simulating stochastic reactive phenomena.

In summary of the detailed analysis for a 'go' versus 'no-go' case, material that is shocked early on and that remains at pressure will evolve into a non-uniform distribution in each cell. The extreme states or "tails" in the pdf distribution accelerate the evolution of the mean. Slight differences in the tail, especially for marginal detonation waves, will affect how the pdf evolves at later times, as shown in Fig. 11. In this case, a 'go' likely results from having more outliers in the right-

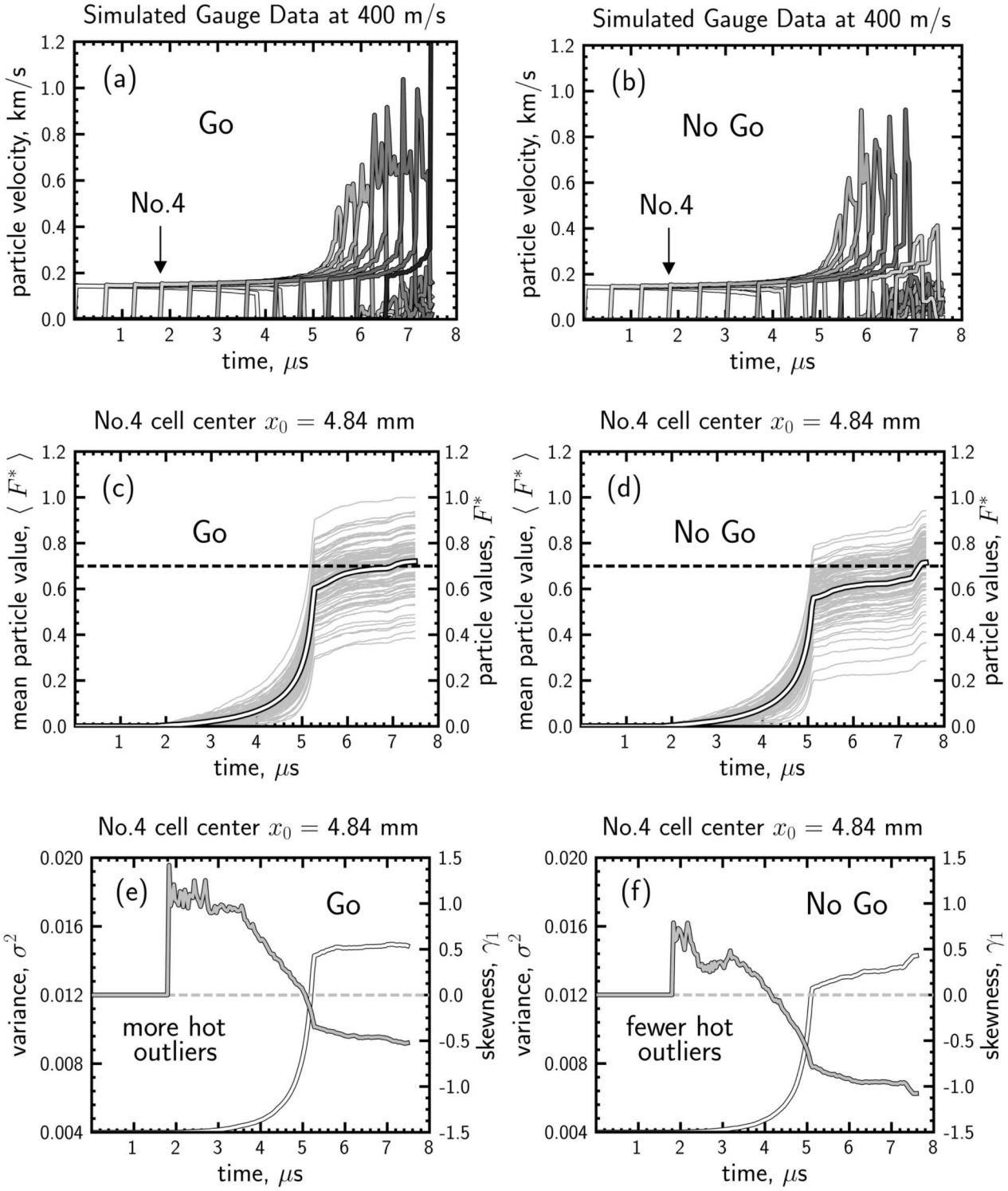

Figure 11. Lagrangian simulation results for a go/no-go comparison. The 'go' case has a calculated run distance of 17.55 mm; the 'no-go' case never exceeds a critical density (4.0 g/cm^3) at the shock front. In (a) and (b), particle velocity histories begin at the flyer/target interface and are spaced at 1.61 mm increments; (c) and (d) show the particle values corresponding to gauge No. 4; (e) and (f) show the variance and skewness as light and dark curves, respectively.

hand tail. Visually, Fig. 11(e) shows a more uniform pdf distribution at 6-7 μs with a higher mean; Fig. 11(f) shows that the pdf is skewed more to the left over this same time. As these particle distributions influence the margins for stochastic initiation, future studies should endeavour to link pdf evolution directly with mesoscale simulations.

4 Ties to the Mesoscale

Results from the stochastic burn model demonstrate that fluctuations in the reaction product mass fraction, F, will propagate into the particle velocity and pressure behind the leading shock wave (e.g. Fig. 3). The net result is the stochastic initiation and propagation behaviour of an otherwise deterministic reactive burn model. The magnitude of the fluctuations in F are not known *a-priori*, and are difficult if not impossible to obtain from experiments; however, it is possible to glean the distribution of F from mesoscale simulations.

Yarrington *et al*. [14] simulated the run-up and failure of detonation in a porous bed of hexanitrostilbene (HNS), with discrete voids randomly distributed throughout the target. The localization of energy at these defects was shown to increase the local temperature, driving the local reaction rates and local product mass fractions – in some cases significantly above the bulk average. Fig. 12 shows the spatial distribution of mass fractions during a flyer impact simulation, which is similar to Ref. [14]. In this simulation, the impact shock generates a relatively high-pressure pulse (~9 GPa) which lasts for approximately 4 ns before the arrival of release waves from the rear of the thin flyer plate. However, the flyer velocity in this simulation is sub-ignition; thus, the shock wave fails to run up to detonation. The local values of product mass fraction, F, show significant variability, from an initial value of zero up to a maximum value of one.

Fig. 13 shows the distribution of F, across a proposed representative volume element or (RVE). The RVE is 8x8 μm, and is illustrated by the dashed box in Fig. 12; the corresponding simulation time for statistical output is 9 ns (τ = 6 ns). Most of the values of F are very low (≤ 10^{-3}), occurring in regions which do not contain hotspots. The mean value of F is relatively high (0.12), and is primarily influenced by the regions which are located at hotspots, some of which have completely reacted (F = 1).

The fluctuations in F are driven by the microstructure, and depend explicitly on the location of defects for the particular microstructure that was simulated. The *moments* of the distribution of F, however, are generalized quantities that would remain constant for statistically similar microstructures. These quantities can be passed directly from mesoscale simulations to the stochastic burn model to calibrate the fluctuations in F. For example, the diffusion coefficient, i.e. B_t^* in Eq. (26), represents the variance of the distribution of F which was hypothesized to decay with time since the passage of the first shock, i.e. τ in Eq. (28). From the mesoscale simulation, the variance of F over the RVE previously described was tracked through time. The arrival time of the shock in this two-dimensional region (refer to Fig. 12) is defined as the time at which the shock reached the centre of the RVE. The variance of F is initially high, as shown in Fig. 14, but then drops rapidly after the shock front passes. Note: the x-axis begins at 2 ns, which is after the initial transient where not all of the RVE has been shocked. Physically, Fig. 14 implies that there is large variability in the local reaction rates early after the shock passes, but the decay rate of hot spot formation leads to fewer fluctuations as time passes.

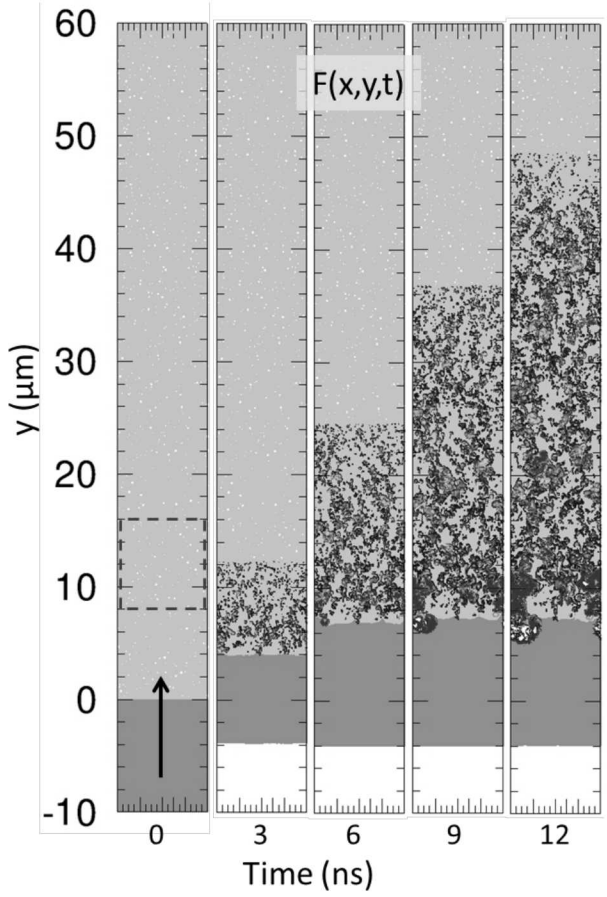

Figure 12. Mesoscale simulation of a flyer impact into a porous bed of HNS showing the evolution of product mass fraction, F. An example of a region of interest for statistical analysis of the distribution is indicated by the dashed box.

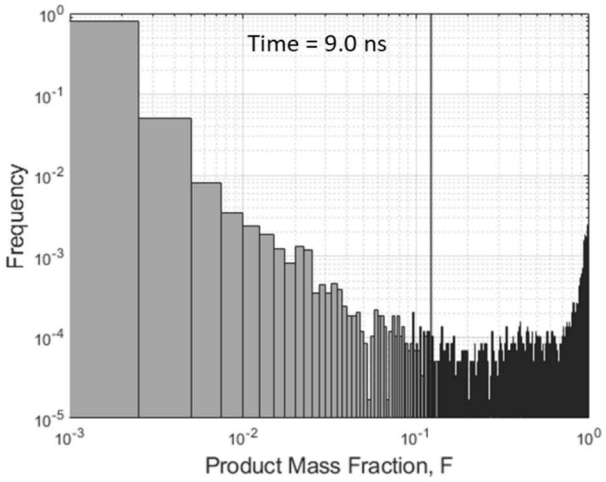

Figure 13. Frequency plot for the product mass fraction, F, at time = 9 ns after impact. The time since passage of the shock across the RVE is 6 ns, and the mean value is indicated by the solid line.

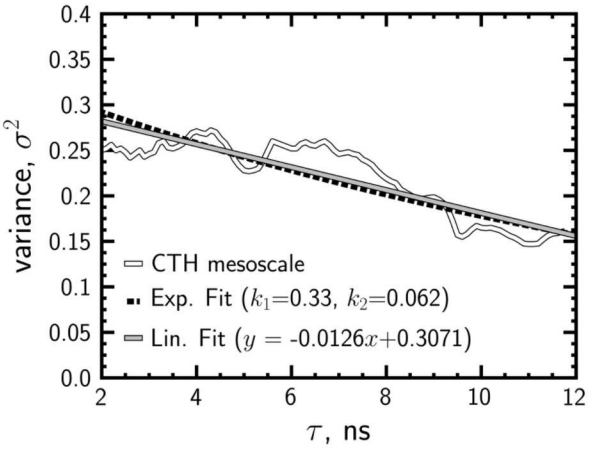

Figure 14. Variance of the distribution of F, with time since passage of the shock. An exponential decay and linear fit are also shown for reference.

Fig. 14 also shows the fit of an exponential decay function, such as the one hypothesized in Eq. (28) with parameters values of k_1 = 0.33 and k_2 = 0.062. The variance from the CTH mesosocale simulation does not necessarily support an exponential decay model, and so a linear fit is also included for comparison which appears to be a better functional form. Such mesoscale calculations are expected to reveal that the true functional form is more complicated than what was postulated in Eq. (28). On the other hand, the mesoscale simulations referred to here were only carried out for a short amount of time, and longer simulation times will reveal more information about the shape of the decay.

The behaviour of the distribution of the product mass fraction, F, is a direct consequence of the microstructural defects in the material which were explicitly modelled in the mesoscale simulations. Local fluctuations, which are deterministic for a fixed microstructure, ultimately give rise to stochastic behaviour when the microstructure is randomly varied (as occurs in nature). The stochastic burn model captures this behaviour by randomly varying the fluctuations in F. Mesoscale simulations may provide a much more physical basis for calibrating the diffusion coefficient decay rate parameters, by linking variations in the microstructure to the stochastic behaviour of explosives during shock initiation.

5 Conclusions

In this work, a new paradigm is put forth for a stochastic reactive burn model that follows directly from our previous letter [1]. Here, it is hypothesized that unreacted material microstructures give rise to a distribution of thermodynamic states, yet these distributions have been missing from the literature on continuum reactive burn models until now. In order to address these distributions with a pdf approach, and to link the meso(grain) and continuum scales for practical calculations, we have extended Lambourn's CIM model with stochastic fluctuations in the product mass fraction/heat release, yield strength, and material impedance. The result is a first-of-its-kind, stochastic burn model for continuum reactive shock waves, and it has been implemented in a one-dimensional research hydrocode. The MOPAC numerical scheme was also developed in order to bypass artificial viscosity, which acts to smear the fluctuations behind the leading shock. In order to fully encapsulate this new stochastic approach, details are given that outline the model derivation, implementation, and numerical convergence.

Following the model development, simulation results are presented for a stochastic shock initiation study consisting of a flyer plate impact scenario. Prompt initiation (i.e. higher shock pressure) leads to a very repeatable run distance to detonation; however, fluctuations are still observed in the particle velocity and pressure histories that are stochastic. This type of reaction-induced variability cannot be obtained using a traditional hydrocode with a deterministic burn model; here, a stochastic burn model utilizes a single set of model parameters that attempts to inform the process-based variability. Multiple repeated runs with the same initial conditions may be used to estimate variations and confidence intervals for the simulation results.

The fundamental stochastic nature of the burn model permits simulations to have varying outcomes with the same initial conditions, and this allows for go/no-go probability estimation. As the shock pressure is lowered on a Pop plot, there is a competition between wave steepening and release. A detailed 'go' versus 'no-go' comparison is made for two simulations at 400 m/s, where it is shown that pdf evolution is heavily influenced by the extreme states in the tails of the pdf distribution. Extra counts in the right-hand tail of the product mass fraction (i.e. more hot outliers) will tip the balance towards initiation rather than detonation failure. As these particle distributions are responsible for marginal reactive behaviour (especially the extreme states and the tails of the pdfs), it is all the more important to have a reasonable way to calibrate them.

Future models will seek to include additional fluctuating variables that may be related to hot spot growth and formation, such as the material porosity, or mechanical damage for simulating fracture, or even a fluctuating temperature field under shock loading. While these future models may or may not follow the current derivation, the underlying approach of the propagation of drift and diffusion coefficients should hold the same. Another direction will be to replace the Lee-Tarver rate law [38] with a modern burn model such as CREST, SURF, AWSD, SHS, etc. [22] to capture the smoothed reaction "hump" feature in greater detail. As new terms are introduced into the stochastic model, the underlying numerical methods will be improved as well, with the ultimate aim of a higher-dimensional 2D or 3D code implementation; this will likely require the development of mesh-free methods for advection. Finally, our discussion of possible future models assumes a differential approach with Langevin-type equations, yet an equivalent integral approach based on Fokker-Planck equations should be considered as well.

Regarding model calibration, many experiments utilize continuum gauge measurements, and this prohibits measuring the pdfs (or variance, skewness, etc.) directly. However, it may be possible to use the measured confidence intervals from certain go/no-go experiments to at least validate the diffusion coefficient parameters. Moreover, the rich statistical datasets from mesoscale calculations may hold the key to informing the underlying pdfs; one such example is shown for a porous HNS explosive. In particular, the mesoscale simulation is used to compute the time-dependent variance in a single RVE, which can then inform the diffusion (i.e. noise) term of the Langevin rate Eq. (26). This mesoscale simulation is an extension from Ref. [14], and shows that the hypothesized exponential decay function will likely be revised for real materials. While such preliminary mesoscale studies inform our future directions, the development of a robust scale-bridging link remains a community endeavour. Stochastic reactive burn models will most likely require full-field data mining, pdf evolution, or even pattern recognition and machine learning to fit the stochastic diffusion coefficient.

Overall, stochastic process modelling is applied with the intent to show these new model capabilities to the EM community. Such capabilities are not present in a traditional hydrocode/continuum burn model, and they should be developed further to allow for predictions of ignition threshold, marginal and failed detonation waves in the shock regime. Stochastic process modelling also represents a clear paradigm shift, one that moves away from deterministic continuum reactive burn models. After performing many mesoscale calculations, it became evident to the authors that the unique insights gained at the mesoscale must have a stronger connection to continuum burn models, and the pdf distributions are hypothesized to link the meso(grain) and the continuum scales with great possibilities.

Aknowledgements

The authors wish to thank Mike Hobbs, Bill Erikson, Robert Knepper, and Judy Brown (SNL) for many useful discussions and critiques of the work. This paper describes objective technical results and analysis. Any subjective views or opinions that might be expressed in the paper do not necessarily represent the views of the U.S. Department of Energy or the United States Government. This work is supported by the Laboratory Directed Research and Development program at Sandia National Laboratories, a multi-mission laboratory managed and operated by National Technology and Engineering Solutions of Sandia, LLC, a wholly owned subsidiary of Honeywell International, Inc., for the U.S. Department of Energy's National Nuclear Security Administration under contract DE-NA0003525.

References

[1] D. E. Kittell, C. D. Yarrington, J. B. Lechman, M. R. Baer, Modeling reactive shock waves in heterogeneous solids at the continuum level with stochastic differential equations, *Phys. Fluids* **2018**, 30, 051701.

[2] M. R. Baer, Modeling heterogeneous energetic materials at the mesoscale, *Thermochim. Acta* **2002**, 384, 351-367.

[3] M. R. Baer, D. K. Gartling, P. E. DesJardin, Probabilistic models for reactive behavior in heterogeneous condensed phase media, *Combust. Theory Modell.* **2012**, 16, 75-106.

[4] R. Hull, P. Keblinski, D. Lewis, A. Maniatty, V. Meunier, A. A. Oberai, C. R. Picu, J. Samuel, M. S. Shephard, M. Tomozawa, D. Vashishth, S. Zhang, Stochasticity in materials structure, properties, and processing–A review, *Appl. Phys. Rev.* **2018**, 5, 011302.

[5] K. Matouš, M. G. D. Geers, V. G. Kouznetsova, A. Gillman, A review of predictive nonlinear theories for multiscale modeling of heterogeneous materials, *J. Comp. Phys.* **2017**, 330, 192-220.

[6] F. P. Bowden, A. D. Yoffe, Initiation and Growth of Explosion in Liquids and Solids, Cambridge University Press, New York, **1952**.

[7] A. W. Campbell, W. C. Davis, J. B. Ramsay, J. R. Travis, Shock initiation of solid explosives, *Phys. Fluids* **1961**, 4, 511-521.

[8] H. Moulard, J. W. Kury, D. Delclos, The effect of RDX particle size on the shock sensitivity of cast PBX formulations, 8th Symposium (International) on Detonation, Albuquerque, NM, USA, July 15-19, **1985**, p. 902.

[9] B. A. Khasainov, B. S. Ermolaev, H.-N. Presles, P. Vidal, On the effect of grain size on shock sensitivity of heterogeneous high explosives, *Shock Waves* **1997**, 7, 89-105.

[10] C. A. Honodel, J. R. Humphrey, R. C. Weingart, R. S. Lee, P. Kramer, Shock initiation of TATB formulations, 7th Symposium (International) on Detonation, Annapolis, MD, USA, June 16-19, **1981**, p. 425.

[11] R. Lee, G. Bloom, W. Von Holle, R. Weingart, L. Erickson, S. Sanders, C. Slettevold, R. McGuire, The relationship between the shock sensitivity and the solid pore sizes of TATB powders pressed to various densities, 8th Symposium (International) on Detonation, Albuquerque, NM, USA, July 15-19, **1985**, p. 3.

[12] N. K. Rai, H. S. Udaykumar, Mesoscale simulation of reactive pressed energetic materials under shock loading, *J. Appl. Phys.* **2015**, 118, 245905.

[13] T. L. Jackson, A. M. D. Jost, J. Zhang, P. Sridharan, G. Amadio, Multi-dimensional mesoscale simulations of detonation initiation in energetic materials with density-based kinetics, *Combust. Theory Modell.* **2018**, 22, 291-315.

[14] C. D. Yarrington, R. R. Wixom, D. L. Damm, Shock interactions with heterogeneous energetic materials, *J. Appl. Phys.* **2018**, 123, 105901.

[15] S. Kim, Y. Wei, Y. Horie, M. Zhou, Prediction of shock initiation thresholds and ignition probability of polymer-bonded explosives using mesoscale simulations, *J. Mech. Phys. Solids* **2018**, 114, 97-116.

[16] Y. Wei, S. Kim, Y. Horie, M. Zhou, Quantification of probabilistic ignition thresholds of polymer-bonded explosives with microstructure defects, *J. Appl. Phys.* **2018**, 124, 165110.

[17] A. Keyhani, S. Kim, Y. Horie, M. Zhou, Energy dissipation in polymer-bonded explosives with various levels of constituent plasticity and internal friction, *Comput. Mater. Sci.* **2019**, 159, 136-149.

[18] A. Nassar, N. K. Rai, O. Sen, H. S. Udaykumar, Modeling mesoscale energy localization in shocked HMX, part I: machine-learned surrogate models for the effects of loading and void sizes, *Shock Waves* **2018,** https://doi.org/10.1007/s00193-018-0875-4.

[19] L. W. Perry, B. Clements, X. Ma, J. T. Mang, Relating microstructure, temperature, and chemistry to explosive ignition and shock sensitivity, *Combust. Flame* **2018**, 190, 171-176.

[20] O. Sen, N. K. Rai, A. S. Diggs, D. B. Hardin, H. S. Udaykumar, Multi-scale shock-to-detonation simulation of pressed energetic material: a meso-informed ignition and growth model, *J. Appl. Phys.* **2018**, 124, 085110.

[21] Y. R. Liu, X. M. Hu, Z. P. Duan, Z. Y. Zhang, A mesoscopic reaction rate model for shock-to-detonation of PBX explosives having different mean particle sizes, *Shock Waves* **2018**, https://doi.org/10.1007/s00193-018-0875-4.

[22] C. A. Handley, B. D. Lambourn, N. J. Whitworth, H. R. James, W. J. Belfield, Understanding the shock and detonation response of high explosives at the continuum and meso scales, *Appl. Phys. Rev.* **2018**, 5, 011303.

[23] S. B. Pope, PDF methods for turbulent reactive flows, *Prog. Energy Combust. Sci.* **1985**, 11, 119-192.

[24] S. B. Pope, Lagrangian PDF methods for turbulent reactive flows, *Annu. Rev. Fluid Mech.* **1994**, 26, 23-63.

[25] J. Doucet, F. Bertrand, J. Chaouki, A measure of mixing from Lagrangian tracking and its application to granular and fluid flow systems, *Chem. Eng. Res. Des.* **2008**, 86, 1313-1321.

[26] M. D. Carrara, P. E. DesJardin, A filtered mass density function approach for modeling separated two-phase flows for LES I: mathematical formulation, *Int. J. Multiphase Flow* **2006**, 32, 365-384.

[27] M. D. Carrara, P. E. DesJardin, A filtered mass density function approach for modeling separated two-phase flows for LES II: simulation of a droplet laden temporally developing mixing layer, *Int. J. Multiphase Flow* **2008**, 34, 748-766.

[28] J. Bakarji, D. M. Tartakovsky, On the use of reverse Brownian motion to accelerate hybrid simulations, *J. Comput. Phys.* **2017**, 334, 68-80.

[29] J. K. Brennan, M. Lísal, J. D. Moore, S. Izvekov, I. V. Schweigert, J. P. Larentzos, Coarse-grain model simulations of nonequilibrium dynamics in heterogeneous materials, *J. Phys. Chem. Lett.* **2014**, 5, 2144-2149.

[30] T. I. Mattox, J. P. Larentzos, S. G. Moore, C. P. Stone, D. A. Ibanez, A. P. Thompson, M. Lisal, J. K. Brennan, S. J. Plimpton, Highly scalable discrete-particle simulations with novel coarse-graining: accessing the microscale, *Mol. Phys.* **2018**, 116, 2061-9.

[31] G. Faure, J.-B. Maillet, Simulations of detonation waves with smoothed dissipative particle dynamics, *arXiv preprint* **2017**, arXiv:1709.03890.

[32] B. Øksendal, Stochastic Differential Equations, Springer Science & Business Media, **2003**.

[33] H. R. James, B. D. Lambourn, On the systematics of particle velocity histories in the shock-to-detonation transition regime, *J. Appl. Phys.* **2006**, 100, 084906.

[34] B. D. Lambourn, An Interpretation of Particle Velocity Histories during Growth to Detonation, *AIP Conf. Proc.* **2003**, 706, 367-370.

[35] B. D. Lambourn, The hydrodynamics of the early stages of the shock to detonation transition, Thirteenth International Detonation Symposium, Norfolk, VA, USA, July 23-28, **2006**, p. 751.

[36] W. Fickett, W. C. Davis, Detonation Theory and Experiment, University of California Press (Dover Ed), Berkeley, USA, **1979**.

[37] E. F. Toro, Riemann Solvers and Numerical Methods for Fluid Dynamics: A Practical

Introduction, Springer Science & Business Media, **1997**.

[38] E. L. Lee, C. M. Tarver, Phenomenological model of shock initiation in heterogeneous explosives, *Phys. Fluids* **1980**, 23, 2362-72.

[39] J. L. Jordan, M. R. Baer, Mixture model for determination of shock equation of state, *J. Appl. Phys.* **2012**, 111, 083516.

[40] P. A. W. Lewis, A. S. Goodman, J. M. Miller, A pseudo-random number generator for the System/360, *IBM Syst. J.* **1969**, 8, 136-146.

[41] R. L. Gustavsen, S. A. Sheffield, R. R. Alcon, Measurements of shock initiation in the tri-amino-tri-nitro-benzene based explosive PBX9502: Wave forms from embedded gauges and comparison of four different material lots, *J. Appl. Phys.* **2006**, 99, 114907.

[42] M. Muradoglu, P. Jenny, S. B. Pope, D. A. Caughey, A consistent hybrid finite-volume/particle method for the PDF equations of turbulent reactive flows, *J. Comput. Phys.* **1999**, 154, 342-371.

[43] J. J. Dick, C. A. Forest, J. B. Ramsay, W. L. Seitz, The Hugoniot and shock sensitivity of a plastic-bonded TATB explosive PBX 9502, *J. Appl. Phys.* **1988**, 63, 4881.

Received: June 22, 2019
Revised: October 1, 2019